INTERNATIONAL JOURNAL FOR NUMERICAL METHODS IN FLUIDS, VOL. 8, 1523–1541 (1988)

HEAT EXCHANGER ANALYSIS ON A MICROVAX II/GPX

ALAN F. HAUGHT

United Technologies Research Laboratories, East Hartford, Connecticut 06108, U.S.A.

SUMMARY

The finite element code FIDAP was used to examine the fluid flow path within a flat plate tube/fin heat exchanger and the resulting heat transfer from the fins and tube walls. The mathematical formulation, mesh development and analysis procedure are presented, and the results obtained are compared with experimental observations of the fluid flow and measurements of the fluid heating. This problem illustrates the capabilities of finite element techniques for analysing complex three-dimensional convection-dominated heat transfer, and demonstrates the scope of problems which can be addressed on a Micro VAX II/GPX workstation.

KEY WORDS Heat exchanger Three-dimensional flow Finite elements FIDAP

INTRODUCTION

Extended surfaces in the form of fin plates are frequently used to augment the heat transfer from heat exchanger tubes. The problem addressed here is the air flow and heating in a single tube row heat exchanger with flat plate fins as illustrated in Figure 1. In the absence of the tubes the air flow through the channels formed by the parallel plate fins would be a simple two-dimensional flow with a developing velocity and thermal boundary layer at the channel entrance. In the absence of the fin plates the flow would be two-dimensional over the tube bank. With both tubes and fins present the flow is highly three-dimensional, with interacting secondary flows of opposite vorticity

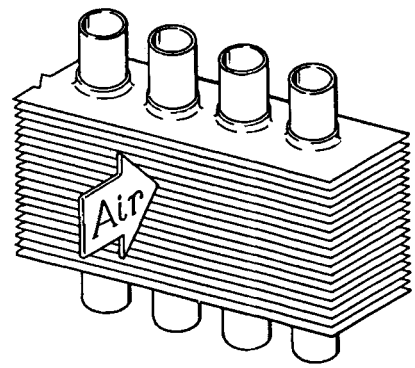

Figure 1. Tube/fin heat exchanger

0271–2091/88/121523–19$09.50

Received 4 December 1987
Revised 22 February 1988

at the front and side of the tubes and a recirculating tube wake, all of which affect the fluid flow path and heating.

For the model tube/fin heat exchanger considered in this analysis, the tube axes are spaced two tube diameters apart, the fin is two tube diameters long in the flow direction, the tube diameter is five times the fin spacing (midfin to midfin) and the fin thickness is 1/16 of the fin spacing. The upstream fluid is at temperature T_0 and has a uniform velocity U along the x-direction. The fluid velocity is zero (no slip) at the fin and tube wall surfaces which are at temperature T_1.

MATHEMATICAL FORMULATION

The heat exchanger geometry and computational domain for the problem are shown in Figure 2. For convenience all of the geometric dimensions are shown in terms of the plate spacing, and in the figure distances along the z-axis are magnified by a factor of two for clarity. The problem is mirror symmetric about four planes: the xz-plane through a tube axis, the xz-plane midway between two adjacent tubes, the xy-plane through the midplane of a fin and the xy-plane midway between two adjacent fins. For computational efficiency the problem is solved for the region within these four planes external to the fin plate and tube and extending one tube diameter in front of and behind the fin to allow for the flow entrance and exit development.

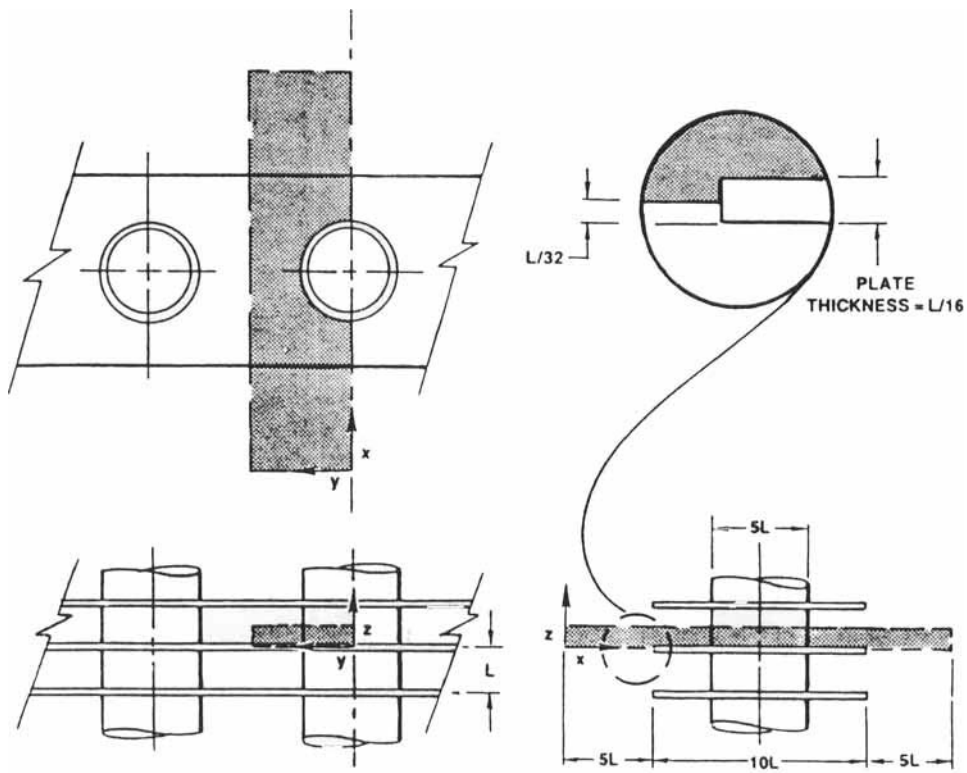

Figure 2. Computational domain (note: dimensions in z-direction magnified $\times 2$)

Field equations

Assuming steady-state incompressible fluid flow with negligible viscous dissipation, the field equations for the problem are the continuity, momentum and energy equations. The equations, in vector form, are

$$\nabla\cdot\mathbf{u}=0, \tag{1}$$

$$\rho\mathbf{u}\cdot\nabla\mathbf{u}=-\nabla p+\mu\nabla^2\mathbf{u}, \tag{2}$$

$$\rho c_p\mathbf{u}\cdot\nabla T=k\nabla^2 T, \tag{3}$$

where

$$\begin{aligned}&\mathbf{x}=\text{distance},\\ &\mathbf{u}=\text{velocity},\\ &\rho=\text{density},\\ &p=\text{pressure},\\ &T=\text{temperature},\\ &\mu=\text{viscosity},\\ &c_p=\text{specific heat},\\ &k=\text{thermal conductivity},\end{aligned} \tag{4}$$

all in consistent units.

The fluid inflow velocity, U, the temperature difference between the upstream fluid and the heat exchanger surfaces, T_1-T_0, the midplane to midplane distance between adjacent fins, L, and the fluid properties serve as reference values for casting the problem in dimensionless form. Multiplying equation (1) by L/U, equation (2) by $L/\rho U^2$, scaling T in equation (3) by the additive constant $-T_0$ and multiplying the resulting equation by $L/\rho c_p U(T_1-T_0)$ (and multiplying the ∇^2 terms in equations (2) and (3) by the additional factor of unity in the form of L/L) results in the following set of dimensionless field equations equivalent to equations (1)–(3):

$$\nabla\cdot\mathbf{u}^*=0, \tag{5}$$

$$\mathbf{u}^*\cdot\nabla\mathbf{u}^*=-\nabla p^*+\frac{1}{Re}\nabla^2\mathbf{u}^*, \tag{6}$$

$$\mathbf{u}^*\cdot\nabla T^*=\frac{1}{Re\,Pr}\nabla^2 T^*, \tag{7}$$

where

$$\begin{aligned}&\mathbf{x}^*=\mathbf{x}/L && =\text{scaled distance},\\ &\mathbf{u}^*=\mathbf{u}/U && =\text{scaled velocity},\\ &\rho^*=1 && =\text{scaled density},\\ &p^*=p/\rho U^2 && =\text{scaled pressure},\\ &T^*=(T-T_0)/(T_1-T_0) && =\text{scaled temperature},\\ &\mu^*=\mu/\rho LU=1/Re && =\text{scaled viscosity},\\ &c_p^*=1 && =\text{scaled specific heat},\\ &k^*=k/\rho LUc_p=1/Re\,Pr && =\text{scaled thermal conductivity}\end{aligned} \tag{8}$$

and

$$Re = \rho LU/\mu, \qquad Pr = \mu c_p/k \tag{9}$$

are the Reynolds number and Prandtl number respectively.

Using the dimensionless equations (5)–(7), the numeric values and fluid properties required are scaled by the relations of equation (8); correspondingly, the results obtained may be interpreted in any consistent system of units by inverse scaling (e.g. $\mathbf{u} = \mathbf{u}^* U$, $p = p^* \rho U^2$, etc.). In the sections which follow, only the dimensionless equations and scaled parameters will be referred to, and for notational convenience the asterisks will be dropped.

Boundary conditions

On each of the four mirror symmetry planes—$y = 0$ through a tube axis (external to the tube and fin), $y = 5$ midway between that and the next tube, $z = 0$ through a fin midplane (in the region ahead of and behind the fin) and $z = 0{\cdot}5$ midway between that and the adjacent fin—the three flow boundary conditions are that the velocity normal to the plane is zero and the two in-plane components of the total shear stress on the plane are each zero. The latter two conditions are equivalent to setting equal to zero the derivatives normal to the plane of the two in-plane velocities. For example, on the xy-plane, $z = 0{\cdot}5$, the boundary conditions are $u_z = \tau_{xz} = \tau_{yz} = 0$. From $\tau_{xz} = \mu(\partial u_z/\partial x + \partial u_x/\partial z) = 0$ coupled with $u_z = 0$ in the plane, $\partial u_x/\partial z = 0$. Similarly, combining $u_z = 0$ and $\tau_{yz} = 0$ in the plane gives $\partial u_y/\partial z = 0$. The temperature boundary condition on each of the four symmetry planes is determined by the requirement that the conductive heat flux normal to the plane be zero. Since for this problem the thermal conductivity is constant, on each symmetry plane the derivative of the temperature normal to the plane is constrained to zero. Thus the boundary conditions on the four mirror symmetry planes are

$$\begin{aligned}
&u_y = 0,\ \tau_{xy} = 0,\ \tau_{zy} = 0,\ \partial T/\partial y = 0; && y = 0,\ 0 \leqslant x \leqslant 5,\ 0 \leqslant z \leqslant 0{\cdot}5,\\
&&& y = 0,\ 5 \leqslant x \leqslant 15,\ 1/32 \leqslant z \leqslant 0{\cdot}5,\\
&&& y = 0,\ 15 \leqslant x \leqslant 20,\ 0 \leqslant z \leqslant 0{\cdot}5,\\
&u_y = 0,\ \tau_{xy} = 0,\ \tau_{zy} = 0,\ \partial T/\partial y = 0; && y = 5,\ 0 \leqslant x \leqslant 20,\ 0 \leqslant z \leqslant 0{\cdot}5,\\
&u_z = 0,\ \tau_{xz} = 0,\ \tau_{yz} = 0,\ \partial T/\partial z = 0; && z = 0,\ 0 \leqslant x \leqslant 5,\ 0 \leqslant y \leqslant 5,\\
&&& z = 0,\ 15 \leqslant x \leqslant 20,\ 0 \leqslant y \leqslant 5,\\
&u_z = 0,\ \tau_{xz} = 0,\ \tau_{yz} = 0,\ \partial T/\partial z = 0; && z = 0{\cdot}5,\ 0 \leqslant x \leqslant 20,\ 0 \leqslant y \leqslant 5.
\end{aligned} \tag{10}$$

For no-slip and the specified temperature on the fin and tube wall surfaces

$$\begin{aligned}
u_x = u_y = u_z = 0,\ T = 1; \quad & x = 5,\ 0 \leqslant y \leqslant 5,\ 0 \leqslant z \leqslant 1/32,\\
& 5 \leqslant x \leqslant 15,\ 0 \leqslant y \leqslant 5,\ [(x-10)^2 + y^2]^{1/2} \geqslant 5,\ z = 1/32,\\
& x = 15,\ 0 \leqslant y \leqslant 5,\ 0 \leqslant z \leqslant 1/32,\\
& [(x-10)^2 + y^2]^{1/2} = 5,\ 1/32 \leqslant z \leqslant 0{\cdot}5.
\end{aligned} \tag{11}$$

In the inflow plane, $x = 0$, the flow velocity is U in the x-direction and the fluid temperature is zero, giving as boundary conditions

$$u_x = U,\ u_y = 0,\ u_z = 0,\ T = 0; \quad x = 0,\ 0 \leqslant y \leqslant 5,\ 0 \leqslant z \leqslant 0{\cdot}5. \tag{12}$$

At the outflow boundary, $x=20$, the normal and in-plane stresses across the exit plane are equal to zero and the conductive heat flux normal to the exit plane is zero, i.e. the normal derivative of the temperature is zero:

$$\tau_{xx}=\tau_{yx}=\tau_{zx}=0,\ \partial T/\partial x=0;\quad x=20,\ 0\leqslant y\leqslant 5,\ 0\leqslant z\leqslant 0{\cdot}5, \tag{13}$$

where τ_{xx} is the total normal stress, $-p+2\mu(\partial u_x/\partial x)$.

Mesh development

Three critical regions require attention in the mesh development: the step at the fin front, the region adjacent to the tube wall and the step at the fin back. Near the steps at the fin front and back the mesh size in the yz-plane must be small relative to the step height to allow for the rapidly changing flow velocity around the step. Similarly, near the tube wall the mesh size in radial planes through the tube axis must be small relative to the distance between the fin and the $z=0{\cdot}5$ midplane to resolve the secondary flows at the tube front and side. Figure 3 shows the mesh used for the heat exchanger analysis.

In FIDAP[1] a mesh is generated on an orthogonal IJK logical space grid of unit cell size which is transformed to geometrical space, merging any nodal points that refer to the same location in geometrical space. Logical space may be considered as plastic, with regions of logical space, appropriately deformed by a continuous transformation, glued (merged) together along their boundaries to form the computational mesh domain in geometrical space.

In the entrance region up to and over the fin step, forces in the y-direction may be anticipated to be small and the flow nominally two-dimensional in any xz-plane. A suitable mesh can therefore be generated in the xz-plane (IK logical space) and propagated with the desired resolution in the y-direction (J logical space). Upstream away from the fin step the velocity gradients are small and a relatively coarse mesh may be used for computational efficiency. However, close to the fin step the mesh size must be small compared with the step height to resolve the flow around the step. These two requirements are met by 'folding' the logical space mesh around the step in geometrical space

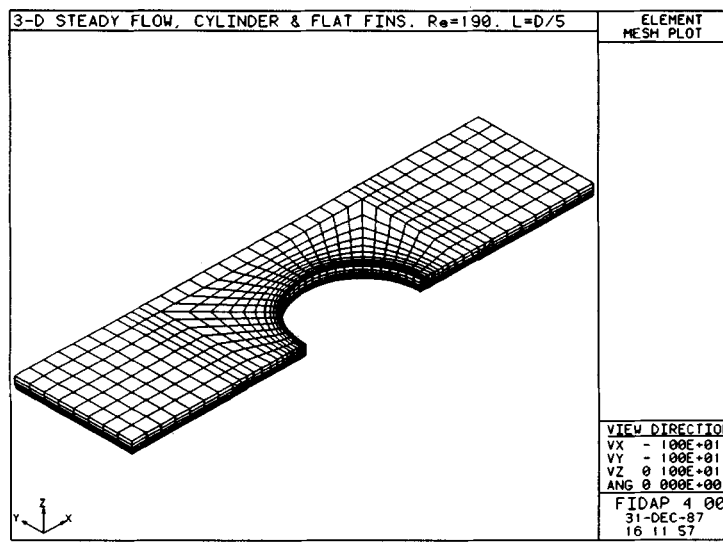

Figure 3. Computational mesh

as shown in Figure 4. Similar considerations apply in the exit region, and the equivalent mesh is generated there.

The same 'folding' is used in the tube region to provide in the xy-plane (IJ logical plane) a fine mesh near the tube surface blended to a coarse mesh away from the tube as shown in Figure 5. The resulting mesh is propagated in the z-direction (K logical space). The exit plane of the entrance region and entrance plane of the tube region, while separate in logical space, are comprised of nodes having the same locations in geometrical space, and the two regions are merged at the

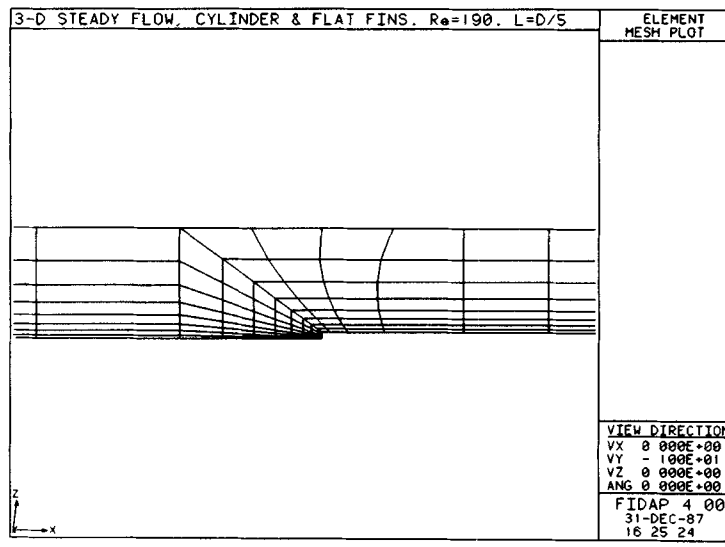

Figure 4. Detail of mesh over step

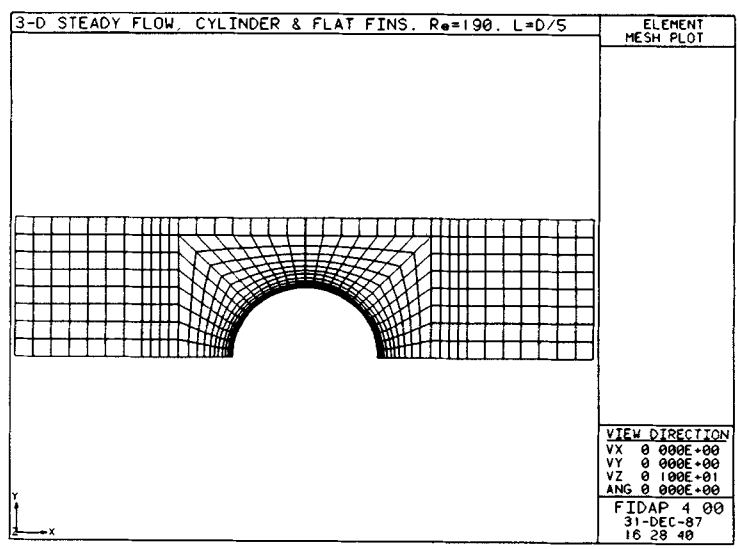

Figure 5. Mesh around tube

interface planes. Similarly, the tube and exit regions are merged to complete the mesh. Eight-node brick elements with trilinear basis functions for the velocity and temperature degrees of freedom and a piecewise constant discontinuous pressure approximation evaluated using a penalty approach are employed for the finite element solution on this mesh.

Analysis procedure

Compared with a 2D problem, a 3D analysis involves a greatly increased number of nodes (the number of nodes in an equivalent 2D problem times the 'depth' resolution), includes an additional velocity (and perhaps pressure as well) degree of freedom and has a vastly increased bandwidth for the solution matrix (determined by the connectivity of adjacent planes rather than lines), all of which combine to increase the solution time much more than might initially be expected. Decreasing the number of degrees of freedom, even by one, can substantially improve the solution time. For the problem considered here the fluid properties are constant and, while the velocity field affects the temperature field through convective effects, the velocity field is not affected by the temperature, i.e. the problem is weakly coupled. However, by first solving for the velocity field as an isothermal problem and using the velocity results as input to an advection–diffusion solution of the energy equation, the number of degrees of freedom during the (lengthy) iteration to convergence is reduced by one, the temperature, with a major reduction in solution time. The advection–diffusion problem with only the temperature degree of freedom requires little time to complete the solution.

The problem is highly non-linear, with secondary flows of opposing vorticity at the front and side of the tube and a large recirculating wake at the rear of the tube. Consequently, starting from a reference velocity field, e.g. the linear Stokes solution, convergence is not readily obtained at Reynolds numbers of interest for the physical problem, 100–400. As a result, the isothermal analysis for the velocity field is attacked in stages, successively decreasing the scaled viscosity ($1/Re$; see equations (8)) until convergence is obtained at the Reynolds number of interest.

Once a convergent solution is obtained at a particular viscosity (Reynolds number), the problem is rerun with a new value of the viscosity (higher Reynolds number), using the velocity field from the previous stage as the first iterate. Because of the sensitivity in obtaining convergence within each stage, the robust successive substitution solution technique is employed. Further, for each iteration the updated solution vector is taken as the average of the present and previous values, i.e. $u_{i+1} = \alpha u_i + (1-\alpha)u$, $\alpha = 0{\cdot}5$, where u is the result obtained with u_i as the iterate. No upwinding was used in the analysis.

The temperature solution is then obtained by rerunning the analysis as an advection–diffusion problem with a thermal conductivity k^* consistent with the flow Reynolds number and the fluid Prandtl number (see equations (8)) and the results from the converged isothermal solution as the input velocity field.

While this analysis process appears convoluted and lengthy, it is much less costly in computer time than a weakly coupled analysis procedure—an important consideration when addressing substantial-size problems with limited computer resources.

COMPUTATIONAL RESULTS

Figures 6–13 illustrate representative results for the flow and temperature fields obtained at a Reynolds number of 190 and a Prandtl number of 0·7. Figure 6 shows the flow field in the $z = 0{\cdot}5$ plane midway between the fin plates, i.e. along the top surface of the region shown in the mesh plot of Figure 3. Separation occurs at about 90° around the tube, and the region behind the tube is

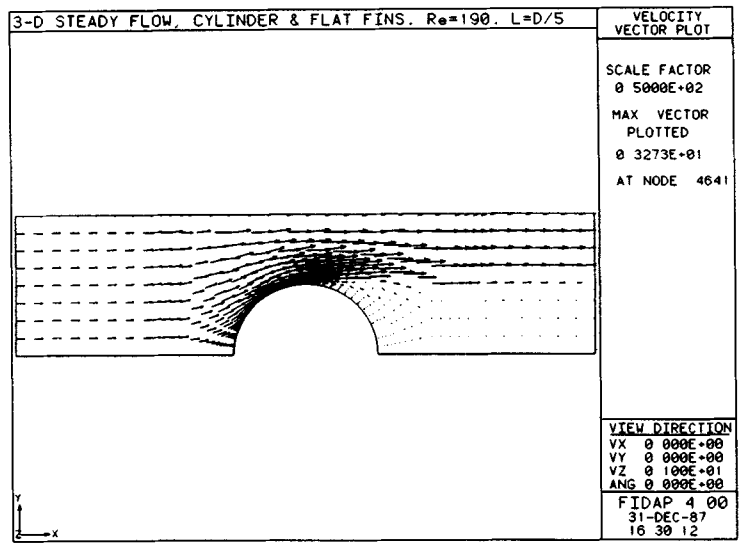

Figure 6. Flow velocity vectors in $z=0{\cdot}5$ plane midway between fins

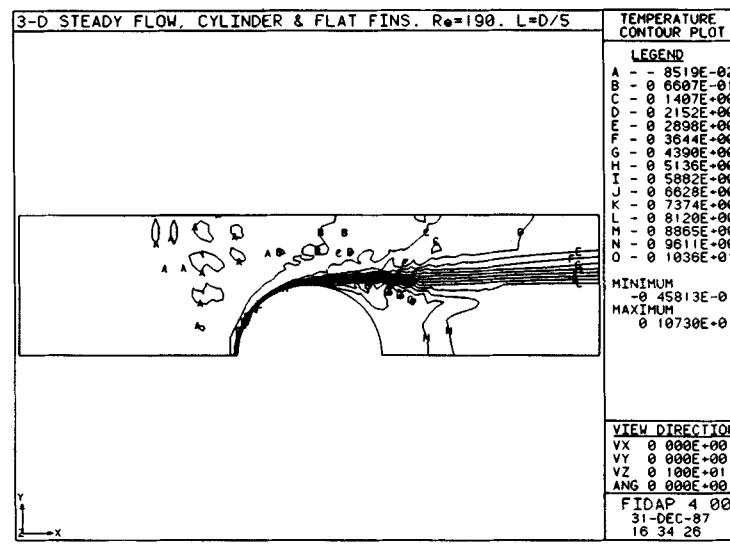

Figure 7. Fluid temperature contours in $z=0{\cdot}5$ plane midway between fins

occupied by a large, very slowly moving recirculation wake. The fluid temperature in the $z=0{\cdot}5$ plane is shown in Figure 7. The thermal boundary layer around the front of the tube, the increasing fluid temperature of the high-speed flow along the $y=5$ line between the tubes and the high temperature of the slowly moving recirculating wake reflect the corresponding features of the flow field. Although the fluid temperature in the wake is high, its velocity is low and little energy is transported downstream from the region behind the tube. Figures 8 and 9 show the flow field and temperature in the $y=0$ plane in front of the tube, viewed from the downstream direction. The

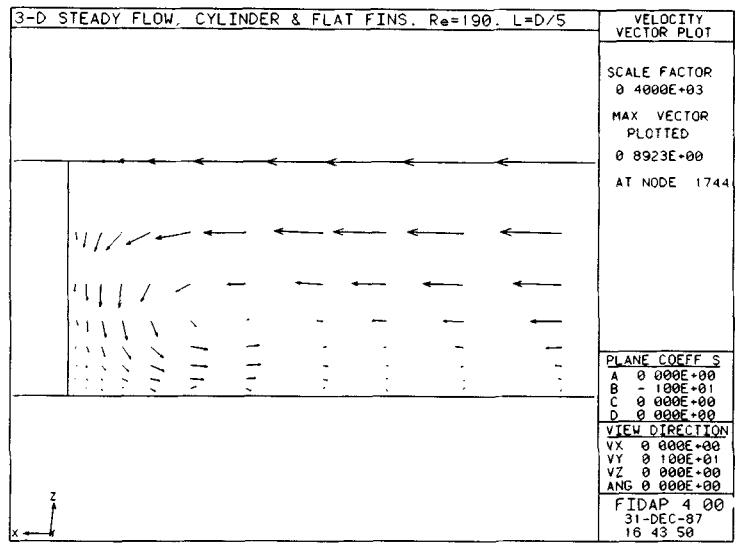

Figure 8. Flow velocity vectors in 0° radial plane

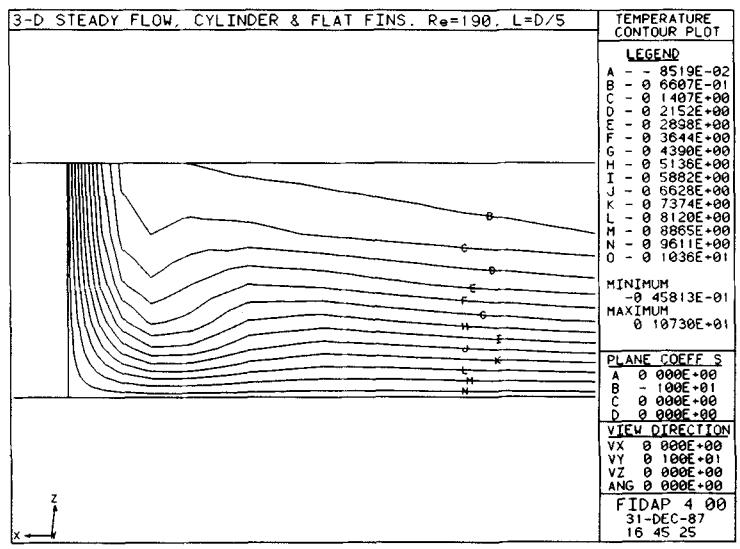

Figure 9. Fluid temperature contours in 0° radial plane

horseshoe vortex evident in the flow plot gives rise to a downturn of the thermal boundary layer over the fin as it nears the front of the tube. In the radial plane 63° around the tube the horseshoe vortex is moved up and away from the tube by the secondary flow of opposite vorticity from the side, and the thermal boundary layer over the tube surface has increased in thickness as shown in Figures 10 and 11. At 90 degrees (Figures 12 and 13) the secondary flow dominates and the tube surface thermal boundary layer is increased further by warm fluid convected by the secondary flow. In Figures 10 and 12 the flow vectors shown represent the fluid velocity in the radial planes

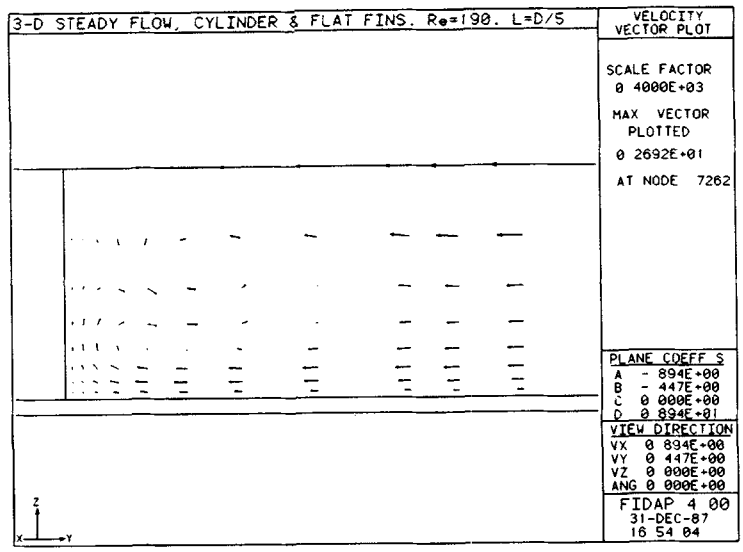

Figure 10. Flow velocity vectors in 63° radial plane

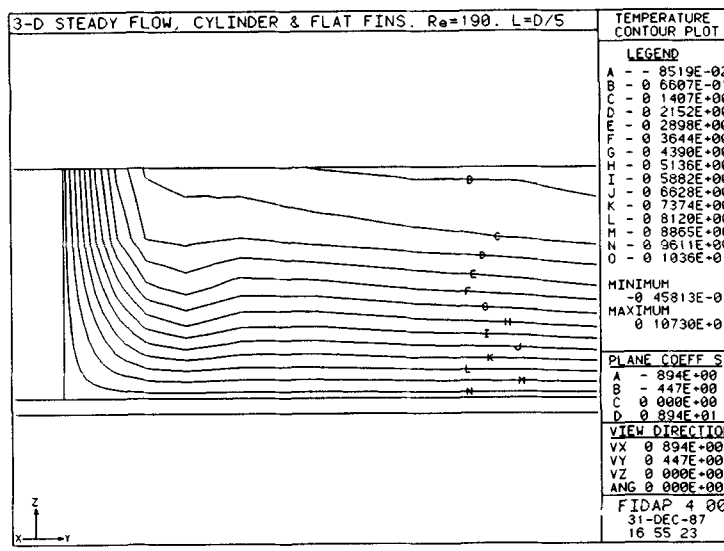

Figure 11. Fluid temperature contours in 63° radial plane

normal to the tube surface; the flow velocity perpendicular to the plane is substantially larger, i.e. the horseshoe and secondary flow vortices are of shallow pitch.

By examining the results at the succession of Reynolds number steps between the Stokes flow starting case and the final Reynolds number value of 190, the influence of flow Reynolds number on the size and configuration of the wake region can be observed. A streamfunction plot as readily calculated for 2D flows is not defined for 3D flow. The qualitative appearance of the wake can be

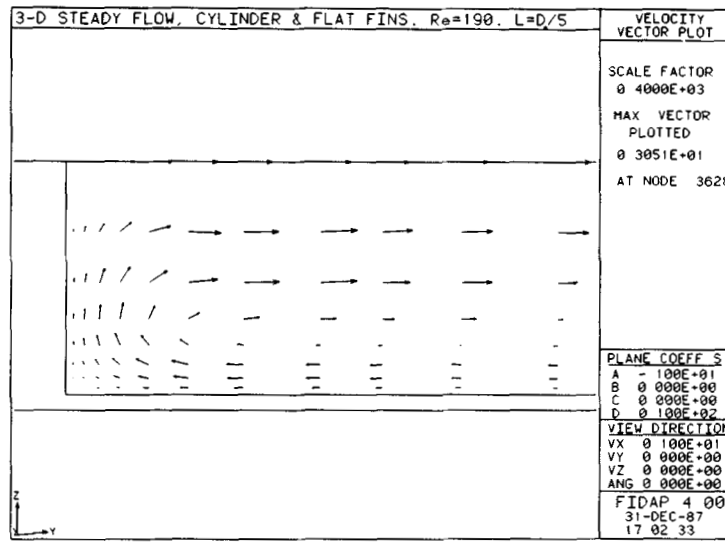

Figure 12. Flow velocity vectors in 90° radial plane

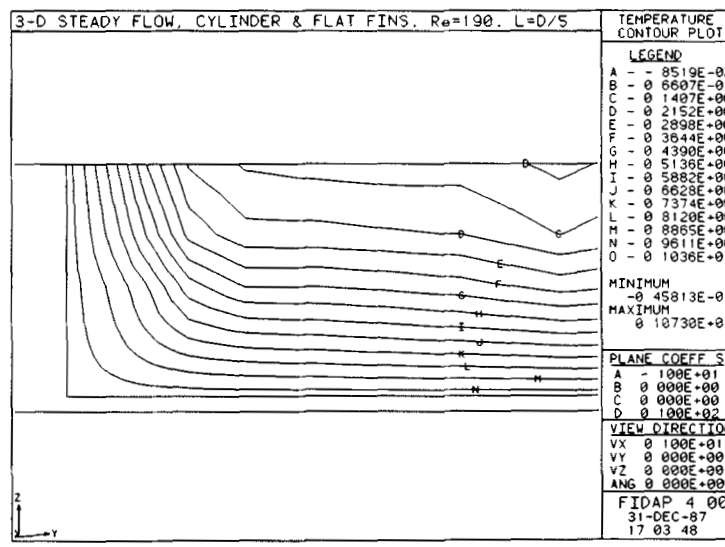

Figure 13. Fluid temperature contours in 90° radial plane

seen from midplane velocity vector displays similar to Figure 6. However, a clearer picture of the extent of the wake is obtained by integrating through the velocity field the path of a fluid element initially located close to the tube centreline in the midplane at the entrance plane ($x=0$, $y=0$, $z=1$). The results of such calculations are shown in Figures 14–17. For Stokes flow the fluid path streamline is symmetric about the tube and no wake is present; the deviation of the path from the tube surface is a measure of the 'error' of this approach introduced by taking a starting point close

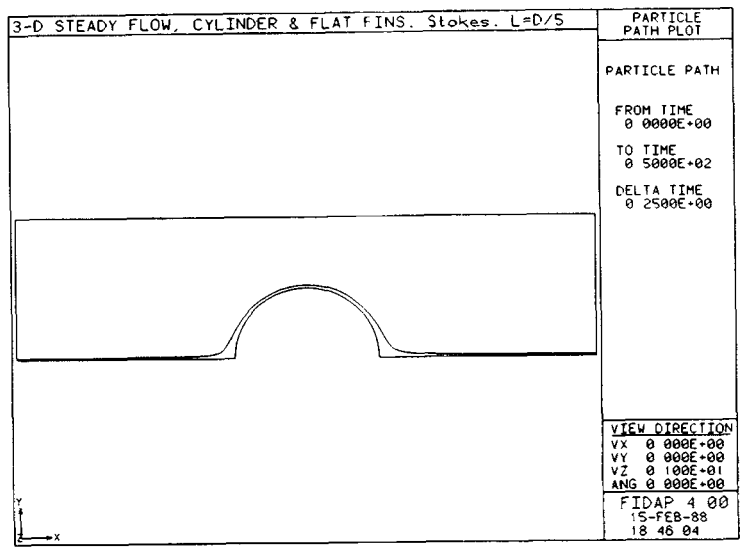

Figure 14. Wake boundary, Stokes flow; no wake present

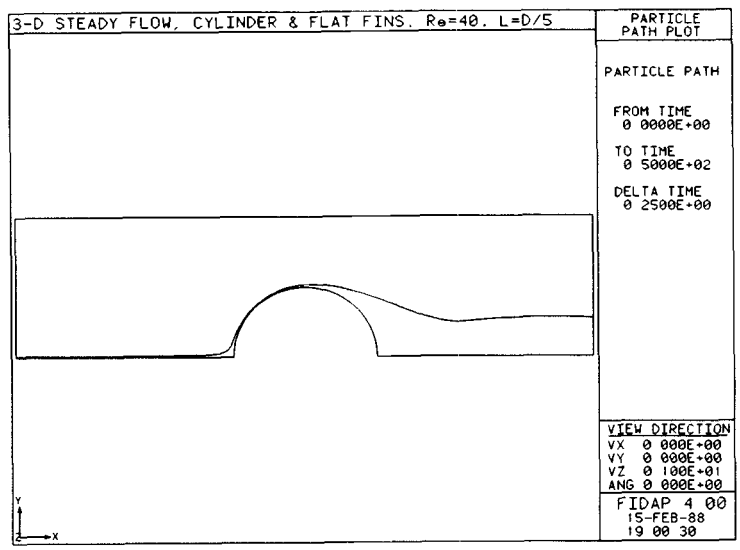

Figure 15. Wake boundary, Reynolds number = 40

to but not at $x=0, y=0, z=1$. At a Reynolds number of 40 the wake is clearly apparent. The wake decreases in width behind the tube back to the rear edge of the fins (located at $D/2$ behind the tube), and then increases slightly to a width of about $D/4$ which persists to the end of the computational domain. At a Reynolds number of 120 the wake width decreases by only a small amount at the rear edge of the fins and is about $D/2$ throughout. At $Re=190$, the velocity vector plot for which is shown in Figure 6, the wake displays a gradual monotonic increase. In all cases for which the wake is present, separation occurs at 90° with no apparent change with Reynolds number. A difference

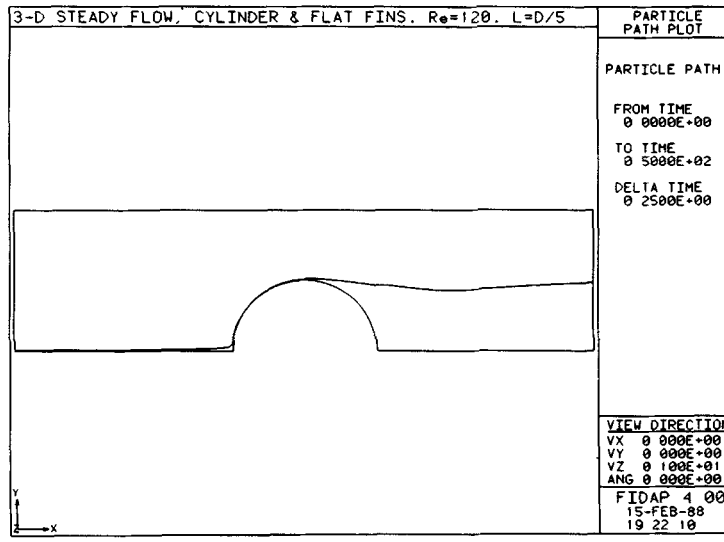

Figure 16. Wake boundary, Reynolds number = 120

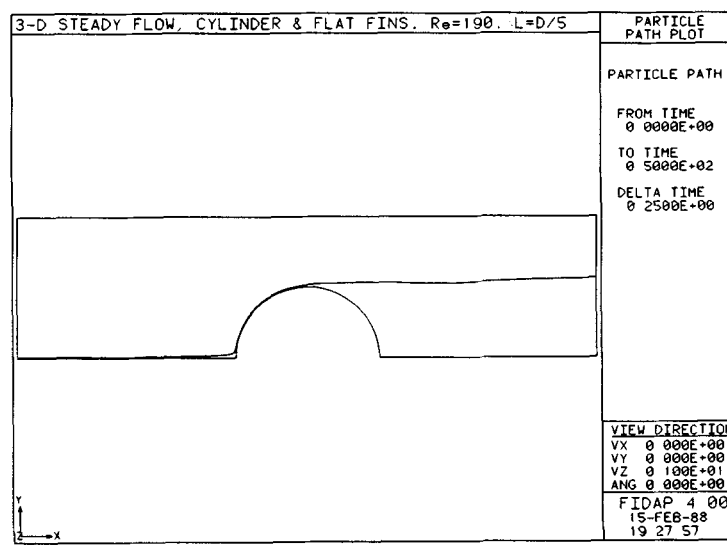

Figure 17. Wake boundary, Reynolds number = 190

in behaviour of the wake within and beyond the fins as observed in Figures 15–17 is not unexpected. Within the plates the flow is constrained by viscous interaction with the fins, while external to the plates that interaction is not present. Indeed, one might expect that the external wake, which is generally similar to the wake behind a 2D obstruction, would break up into the eddies of a vortex street; as discussed below, such behaviour is observed experimentally several tube diameters behind the fins.

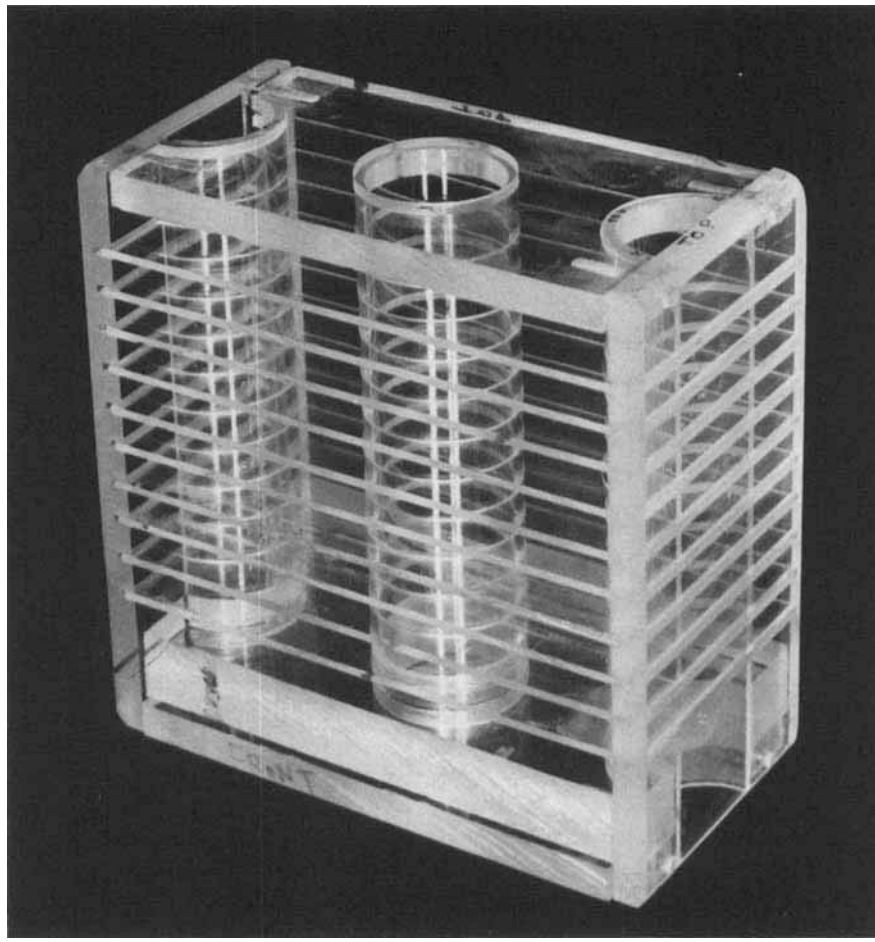

Figure 18. Single tube row flow visualization model

Although the fluid temperature should be bounded by the fluid inflow and wall temperatures, 0 and 1 respectively (dissipation is not included in this analysis), the results show fluid temperatures ranging from −0·05 to 1·07 (see e.g. Figure 7). Such non-physical temperatures occur in regions of alternating convergence and divergence of the fluid flow. These regions display the classical node-to-node oscillatory behaviour (or 'wiggles') frequently encountered with conventional Galerkin finite element methods.[2] The temperature anomalies are a consequence of the convective coupling between the velocity and temperature fields in such regions, and when excessive the velocity oscillations and associated temperature anomalies indicate that further local mesh refinement would be appropriate.

In subsequent calculations with a mesh slightly modified for a wider tube spacing, streamline upwinding was used in an effort to achieve more rapid convergence. The upwinding had the unfortunate effect of causing the solution on successive iterations to alternate between two quite non-physical flow patterns in the wake recirculation region. Upon disabling upwinding, the solution resumed steady convergence to a physically valid result. For 2D flow around a cylinder in a geometry equivalent to the midplane of Figure 3, upwinding and no-upwinding gave indi-

stinguishable results. Because of the length of time required for each iteration of the 3D problem (see Resources), the anomalous behaviour of upwinding in the 3D case has not been explored further.

As in a typical heat exchanger, the plate spacing for this model problem is much smaller than the tube diameter ($L = D/5$) Thus the flow Reynolds number if expressed in terms of the tube diameter would be 950, much greater than the 40–60 threshold for the formation of a time-dependent vortex street in 2D flow over a cylinder. However, in the 3D flow considered here, the fin plates serve to stabilize the flow by viscous interaction, suppressing the vortex shedding and producing a steady flow for which the time-independent analysis employed applies. To test that this was the case for the heat exchanger geometry of the model problem, a single tube row flow visualization model (shown in Figure 18) was constructed of lucite and set up in a water flow tunnel to observe the flow. A dilute suspension of finely ground flakes of mother-of-pearl* dispersed in the water was illuminated by a 2D sheet laser beam to display the flow.[3] Figure 19 is a photograph of the flow pattern obtained with the laser beam midway between two of the fins, i.e. the midplane flow corresponding to the calculated results of Figures 6 and 17. The flow visualization clearly shows a steady flow (i.e. no vortex street) between and immediately behind the fins, validating the use of the steady analysis. Further, the water tunnel flow displays within and behind the fins extending downstream from the tubes a large wake whose configuration is in good agreement with that of Figure 17 predicted by the 3D flow analysis. The apparent necking down of the wake between the tube and rear edge of the plates in the photograph of Figure 19 is an artifact of the still picture and is the manifestation of kidney-shaped secondary recirculation regions just inside the wake boundary, which with scrutiny can also be seen in Figure 6. Beyond about four to five tube diameters behind the fins, the wake begins to break up into eddies—the initiation of a vortex street commensurate with the large tube Reynolds number, $Re_T = \rho UD/\mu$, associated with the flow in the absence of the plates.

Flow velocity and thermal measurements were made in an air tunnel using a 10 × scale, single tube row, flat fin heat exchanger model of similar geometry to that considered in the analysis. Velocity and temperature measurements along the $y = 5$ line and along the $z = 0{\cdot}5$ line in the yz-plane one tube diameter behind the plates ($x = 20$) show qualitatively the wakes of the fins and of the tubes evidenced in the calculated curves of Figures 20–23. However, because of the differences in geometry (specifically, the ratio of tube spacing to tube diameter) between the experimental and analytical configurations, and since fin conduction and the resultant surface temperature variation over the fin were not included in the analysis, simple Reynolds number or other scaling cannot be used to plot the measured values on the analytical curves. Calculations for the experimental geometry and incorporating the effects of fin and tube thermal conductivity are being made in order to provide a direct comparison of the results.

Classically, the problem of low-Reynolds-number flow around cylindrical bodies between two plates normal to the cylinder axis was studied by Hele-Shaw[4, 5] to demonstrate potential flow streamlines. Assuming that viscous forces dominate and that the effect of the plates is to impose a parabolic flow velocity distribution between the plates, the flow streamlines around the body are those of 2D potential flow with a reduced Reynolds number. The Hele-Shaw flow Reynolds number expressed as the ratio of inertia to viscous forces is

$$Re_{HS} = \frac{\rho U^2/D}{\mu U/(L/2)^2} = \frac{\rho UD}{\mu}\left(\frac{L}{2D}\right)^2. \tag{14}$$

* AQ-1000 rheoscopic concentrate, supplied by Kalliroscope Corporation, Groton, MA.

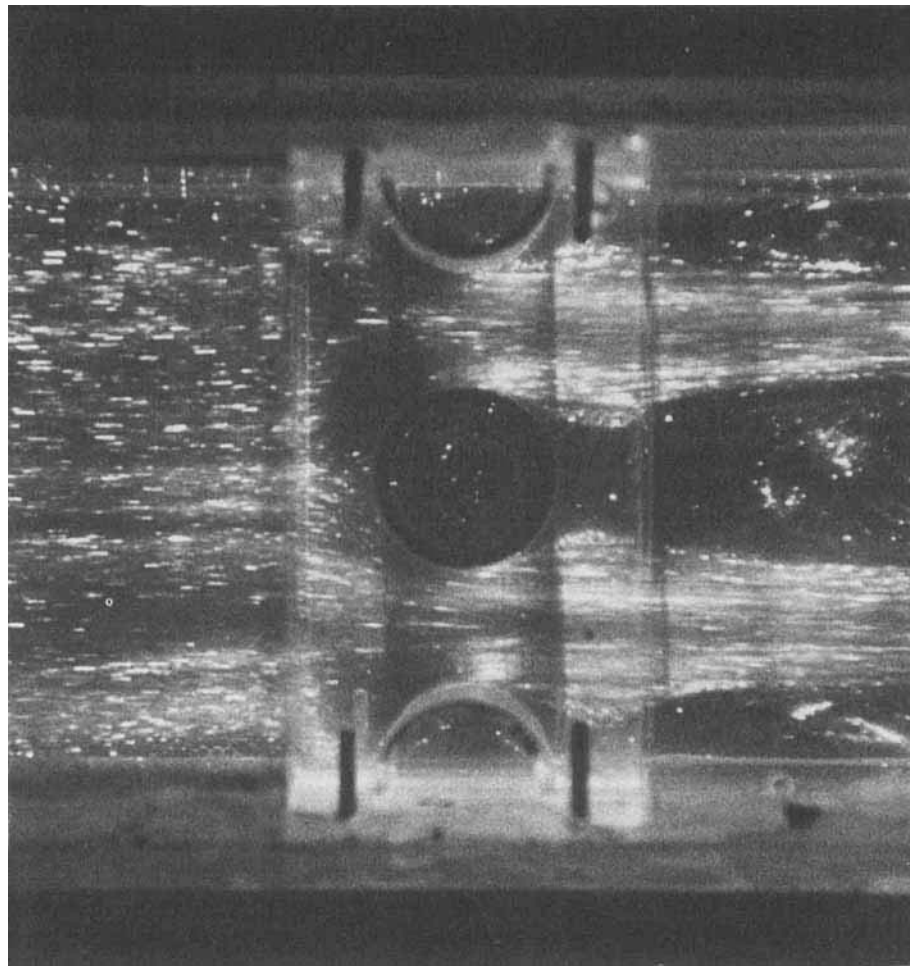

Figure 19. Water tunnel midplane flow; flow is from left to right and illumination is from the far side (top in the photograph)

This is to be compared with the flow Reynolds number expressed in terms of the tube diameter in the absence of the plates, $Re_T = \rho UD/\mu$; the reduction factor $(L/2D)^2$ represents the viscous interaction influence of the plates on the flow. (Note that the Reynolds number of equation (9) used for non-dimensionalizing the field equations is a plate spacing Reynolds number; for a given geometry, i.e. ratios of plate spacing, tube diameter, fin length and tube spacing, any one of the problem length scales could have been chosen as the reference length.) The assumption of a parabolic flow distribution between the plates is consistent with a no-slip boundary condition at the plates but results in a slip boundary condition at the cylindrical body surface. Consequently, the Hele-Shaw flow suppresses not only the secondary flows (i.e. velocities normal to the plates) but also any 'in-plane' recirculation, and as a result does not properly apply to a 3D case for which such flows are substantial, i.e. for Re_{HS} greater than 1.

However, it might be expected that the reduction factor $(L/2D)^2$ would approximately apply even at modest Re_{HS} numbers for which recirculation is significant, and that a 2D analysis using a

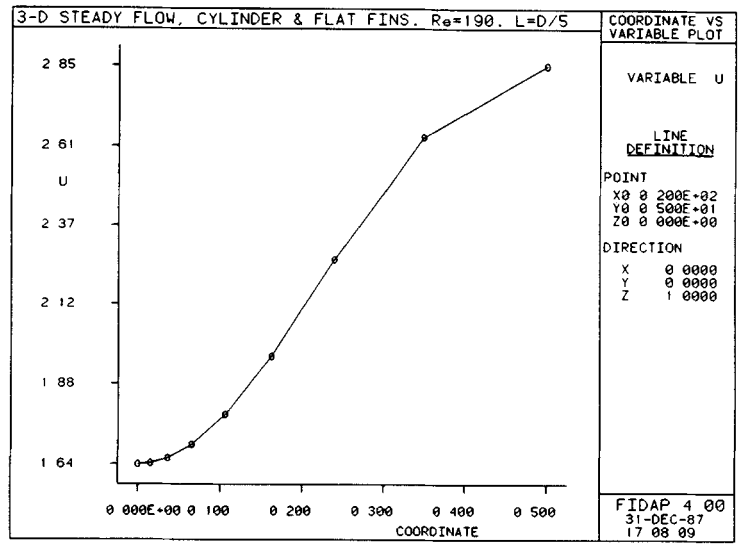

Figure 20. Axial velocity along $y=5$ line in exit plane ($x=20$)

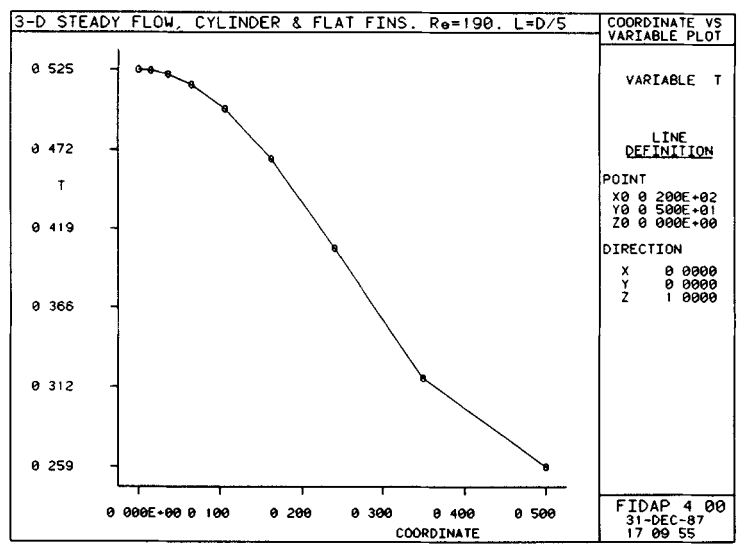

Figure 21. Fluid temperature along $y=5$ line in exit plane ($x=20$)

Reynolds number scaled by $(L/2D)^2$ could provide a general description of the flow. 2D calculations were performed at a reduced Re_T of 10 (i.e. $\sim 950/100$) and compared with the results of the 3D analysis for the 2D flow in the plane midway between the plates. Major differences were observed in the length and size of the recirculation region behind the tube. The 2D reduced Re_T results predict a small recirculation for about $D/4$ behind the tube, while from Figure 17 the 3D calculations display in the midplane a recirculating wake nearly as wide as the tube back to the rear of the plate ($D/2$ away) and persisting thereafter to the end of the computational domain (D behind the plates). As shown by the photograph of Figure 19, the experimental results confirm the

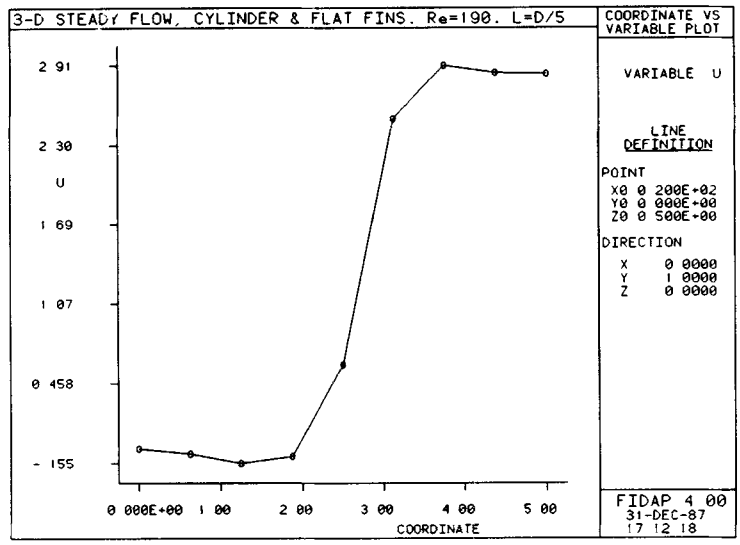

Figure 22. Axial velocity along $z=0{\cdot}5$ line in exit plane ($x=20$)

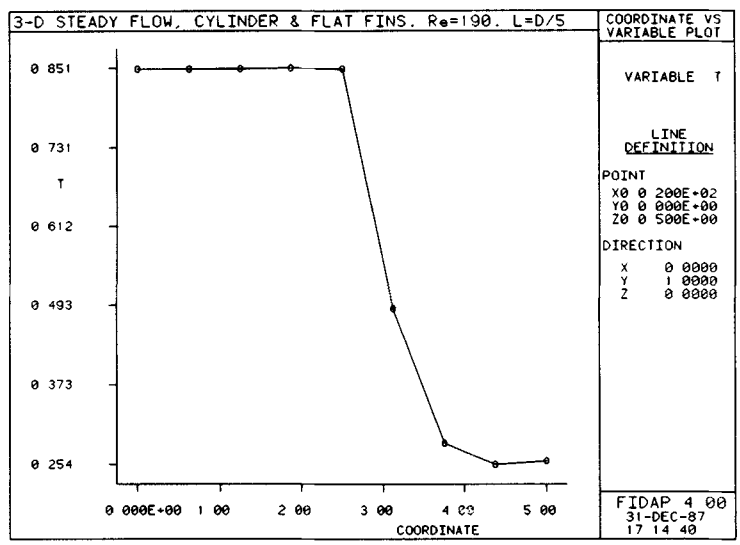

Figure 23. Fluid temperature along $z=0{\cdot}5$ line in exit plane ($x=20$)

predictions of the 3D analysis, and the Hele-Shaw flow reduced Reynolds number cannot be used to estimate the heat exchanger flows in the regimes of interest.

RESOURCES

The computational heat exchanger model involved 5680 elements and 7128 nodes. With FIDAP 3.14 each iteration of the non-linear flow analysis required 11 h of CPU and 14 h of clock time. Using three Reynolds number steps (40, 120 and 190), a total of 18 iterations was required to

obtain a converged solution. Including the advection–diffusion final step (1 h CPU, 1·5 h clock time), the analysis took a total of 250 h of clock time. The analysis was performed on a Micro VAX II/GPX workstation with 13 Mbytes of core memory and 310 Mbytes of disc storage space. It was necessary (and easy) to reconfigure the FIDAP code to use 8 Mbytes of the core memory; the as-supplied memory setting of 0·8 Mbytes was too small for a 3D problem of this size, even though FIDAP utilizes an out-of-core matrix solver. Disc storage space for each saved result occupied 6·5 Mbytes, and approximately 132 Mbytes of disc space was required for the scratch files during each iteration. Unoccupied disc space of the magnitude required for the analysis was not initially available on the workstation. As a result, disc space on another computer was accessed remotely via Ethernet for the scratch files. The scratch files are used for storage of the element and solution matrix data during the calculation, and, because of the large amount of I/O to them with the out-of-core matrix solver, the remote disc access increased the solution time of an iteration by nearly 50% to $\sim$20 h of clock time. Although a problem of this magnitude clearly presses the limits for solution on a Micro VAX II/GPX workstation, by conducting each iteration as an overnight run it was possible to carry out the analysis without interfering with interactive use of the workstation during the day.

Subsequent calculations with the extended capabilities of the latest version of FIDAP (4.0) have shown the value of an adddtional workstation strategy. The solution time for the successive substitution procedure, generally recommended for the early stages of an analysis because of its robust nature and large radius of convergence, scales roughly as the square of the matrix mean bandwidth times the number of degrees of freedom. Reducing the bandwidth and number of degrees of freedom each by a factor of $\sim$2 (e.g. in the problem considered here by changing the number of elements in the z-direction from eight to four) decreases the solution time by a factor of $\sim$8. As a result, as a final check on the mesh connectivity and boundary condition assignments, it is convenient to use a coarse version of the mesh to preview the Stokes and even low-Reynolds-number solutions. Such solutions can uncover set-up errors otherwise difficult to detect: an unintended mismatch where two parts of the mesh are joined together is readily revealed by unexpected fluid outflow in post-processing the coarse mesh solution. Although the coarse mesh may be inadequate for resolving the flow at the Reynolds numbers of ultimate interest, it can provide valid results at low Reynolds numbers. FIDAP 4.0 supports interpolating solutions obtained on one mesh to an equivalent but refined mesh. Thus the coarse mesh low-Reynolds-number results can be used as the starting iterate for a higher-Reynolds-number case on a finer mesh, substantially reducing the computation time. Analysing a 3D problem of this size on a workstation requires careful tracking of the error norms and solution behaviour to select an efficient solution strategy and iteration procedure. The graphics capability of the workstation helps greatly in this process, and as an ancillary benefit provides an intimate familiarity with the developing flow solution.

REFERENCES

1. *FIDAP User's Manual*, Fluid Dynamics International, Inc., Evanston, IL, 1987.
2. P. M. Gresho and R. L. Lee, 'Don't suppress the wiggles—they're telling you something!', *Comput. Fluids*, **9**, 223–255 (1981).
3. P. Matisse and M. Gorman, 'Neutrally buoyant anisotropic particles for flow visualization', *Phys. Fluids*, **27**, 759–760 (1984).
4. H. S. Hele-Shaw, 'Investigation of the nature of surface resistance of water and of stream motion under certain experimental conditions', *Trans. Inst. Naval Arch.*, **IX**, 25 (1898); see also *Nature*, **58**, 34 (1898) and *Proc. Roy. Inst.*, **16**, 49 (1899).
5. H. Schlichting, *Boundary Layer Theory*, McGraw-Hill Book Co., Inc., New York, 1960, pp. 104–106.